The Crystal Structure of *Bacillus cereus* Phosphonoacetaldehyde Hydrolase: Insight into Catalysis of Phosphorus Bond Cleavage and Catalytic Diversification within the HAD Enzyme Superfamily[†,‡]

Marc C. Morais,[§] Wenhai Zhang,[∥] Angela S. Baker,[∥] Guofeng Zhang,[⊥] Debra Dunaway-Mariano,[⊥] and Karen N. Allen*[,§]

Department of Physiology, Structural Biology Group, Boston University School of Medicine, Boston, Massachusetts 02118-2394, Department of Chemistry and Biochemistry, University of Maryland, College Park, Maryland 20742, and Department of Chemistry, University of New Mexico, Albuquerque, New Mexico 87131

Received May 24, 2000

ABSTRACT: Phosphonoacetaldehyde hydrolase (phosphonatase) catalyzes the hydrolysis of phosphonoacetaldehyde to acetaldehyde and phosphate using Mg(II) as cofactor. The reaction proceeds via a novel bicovalent catalytic mechanism in which an active-site nucleophile abstracts the phosphoryl group from the Schiff-base intermediate formed from Lys53 and phosphonoacetaldehyde. In this study, the X-ray crystal structure of the *Bacillus cereus* phosphonatase homodimer complexed with the phosphate (product) analogue tungstate ($K_i = 50$ μM) and the Mg(II) cofactor was determined to 3.0 Å resolution with an $R_{cryst} = 0.248$ and $R_{free} = 0.284$. Each monomer is made up of an α/β core domain consisting of a centrally located six-stranded parallel β-sheet surrounded by six α-helices. Two flexible, solvated linkers connect to a small cap domain (residues 21−99) that consists of an antiparallel, five-helix bundle. The subunit−subunit interface, formed by the symmetrical packing of the two α8 helices from the respective core domains, is stabilized through the hydrophobic effect derived from the desolvation of paired Met171, Trp164, Tyr162, Tyr167, and Tyr176 side chains. The active site is located at the domain−domain interface of each subunit. The Schiff base forming Lys53 is positioned on the cap domain while tungstate and Mg(II) are bound to the core domain. Mg(II) ligands include two oxygens of the tungstate ligand, one oxygen of the carboxylates of Asp12 and Asp186, the backbone carbonyl oxygen of Ala14, and a water that forms a hydrogen bond with the carboxylate of Asp190 and Thr187. The guanidinium group of Arg160 binds tungstate and the proposed nucleophile Asp12, which is suitably positioned for in-line attack at the tungsten atom. The side chains of the core domain residue Tyr128 and the cap domain residues Cys22 and Lys53 are located nearby. The identity of Asp12 as the active-site nucleophile was further evidenced by the observed removal of catalytic activity resulting from Asp12Ala substitution. The similarity of backbone folds observed in phosphonatase and the 2-haloacid dehalogenase of the HAD enzyme superfamily indicated common ancestry. Superposition of the two structures revealed a conserved active-site scaffold having distinct catalytic stations. Analysis of the usage of polar amino acid residues at these stations by the dehalogenases, phosphonatases, phosphatases, and phosphomutases of the HAD superfamily suggests possible ways in which the active site of an ancient enzyme ancestor might have been diversified for catalysis of C−X, P−C, and P−O bond cleavage reactions.

Phosphonates enter the environment through commercial as well as through natural sources. Once thought obscure, phosphonates are now known to play highly specialized roles in the many organisms that synthesize them (*1*−*5*). As chemically stable organophosphate mimetics, phosphonates display a wide range of biological activities that, in recent years, have been exploited in their commercial application as herbicides, pesticides, antibiotics, fungicides, and antiviral agents (*6*). The biodegradative pathways that have evolved in bacteria to recycle natural phosphonates may, with some engineering, serve as a future means to control environmental contamination by this rapidly expanding class of pollutants.

Studies of phosphonate degradation pathways in soil-dwelling bacteria have identified several enzymes specialized in catalysis of hydrolytic P−C bond cleavage. These are the C-P lyase, a ubiquitous and highly complex integral membrane protein system that hydrolyzes a broad spectrum of phosphonate compounds via a homolytic chemical pathway (*7*−*9*), and the phosphonoacetaldehyde hydrolase (*10*), phosphonoacetate hydrolase (*11*), and phosphonopyruvate hydrolase (*12*), each of which is a substrate-specific phosphonohydrolase functioning in heterolytic P−C bond cleavage. Phosphonoacetaldehyde hydrolase (phosphonatase)[1] from *Bacillus cereus* is the topic of this paper.

[†] This work was supported by NIH Grant GM61099-01 to K.N.A. and D.D.-M. Research was carried out (in part) at the HHMI beamline X4A at the National Synchrotron Light Source, Brookhaven National Laboratory.

[‡] The coordinates of the refined structure have been deposited with the Protein Data Bank, accession code 1FEZ.

* Correspondence should be addressed to this author. E-mail: allen@med-xtal.bu.edu, Phone: 617-638-4398, FAX: 617-638-4273.

[§] Boston University School of Medicine.

[∥] University of Maryland.

[⊥] University of New Mexico.

10.1021/bi001171j CCC: $19.00
Published on Web 08/03/2000

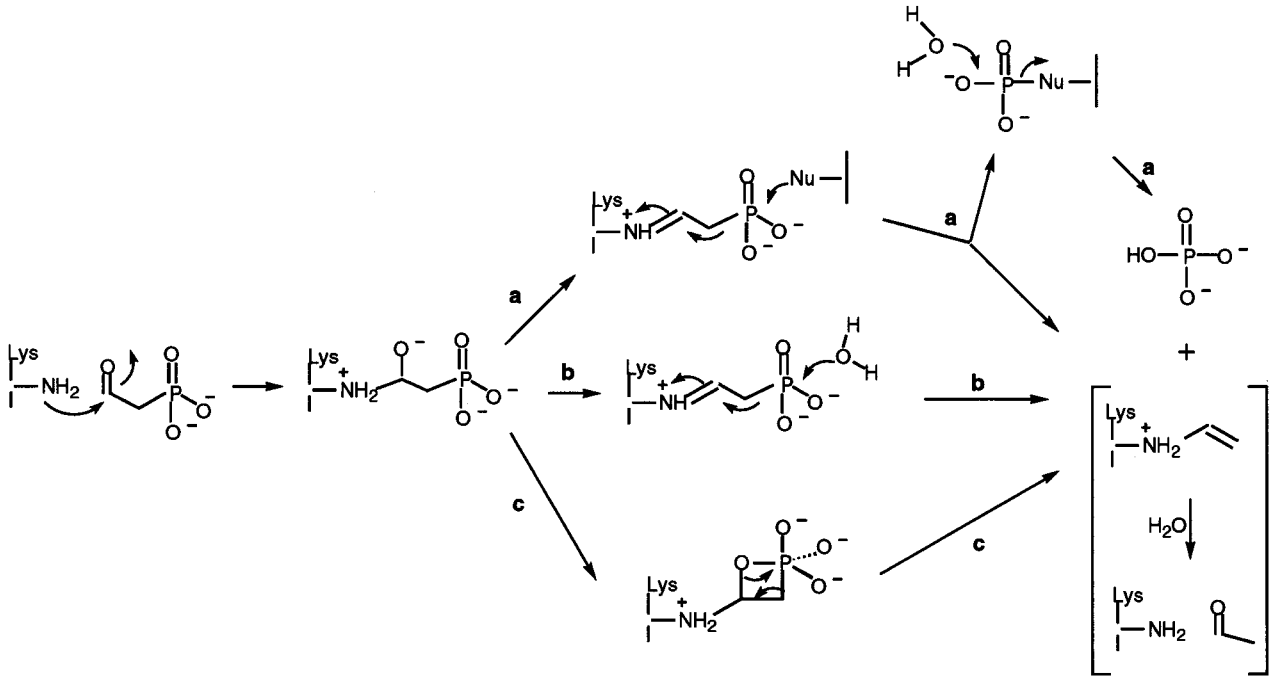

FIGURE 1: Alternative catalytic mechanism for phosphonatase-catalyzed hydrolysis of P-Ald.

Scheme 1: AEP Degradation Pathway (*13, 14*)

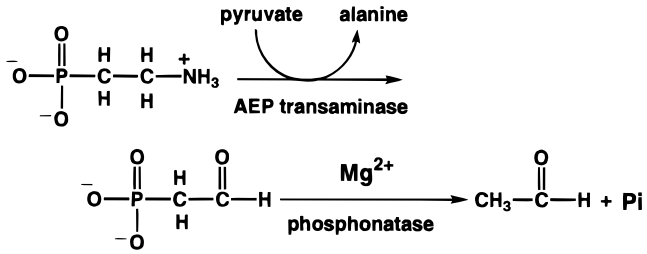

Phosphonatase functions as catalyst in a two-step chemical pathway found in *Pseudomonas aeruginosa*, *Pseudomonas putida*, *Enterobacter aerogenes*, *Bacillus cereus*, *Rhizobium meltoti*, and *Salmonella typhimirium* (*13*−*19*) designed to degrade the ubiquitous natural phosphonate 2-aminoethylphosphonate (AEP)into useable forms of nitrogen, carbon, and phosphorus (Scheme 1). AEP is produced by protozoans such as *Tetrahymena pyriformis* from phosphoenolpyruvate. Small-molecule phosphonates such as AEP are utilized in prokaryotes primarily for chemical warfare while larger AEP adducts of proteins, lipids, and glycans found in eukaryotes are produced for purposes which are presently unknown (*20*, *21*). The first step of the AEP degradation pathway, catalyzed by AEP transaminase, involves the transfer of NH_3 from AEP to pyruvate, yielding phosphonoacetaldehyde (P-Ald) and alanine. In the second step, catalyzed by phosphonatase, P-Ald is hydrolyzed to acetaldehyde and inorganic phosphate.

Phosphonatase has been purified from *Pseudomonas aeruginosa*, *Bacillus cereus*, and *Salmonella typhimirium* (*13*, *15*, *22*). The *B. cereus* enzyme is a stable and soluble homodimeric enzyme of 30 361 Da monomer molecular mass that requires Mg(II) for activity and that is optimally active between pH 6.5 and pH 8.5. Phosphonatase catalyzes the hydrolysis of its natural substrate P-Ald with a $k_{cat} = 15\ s^{-1}$ and $K_m = 33\ \mu M$. Thiophosphonoacetaldehyde ($k_{cat} = 0.7\ s^{-1}$; $K_m = 50\ \mu M$) and acetonylphosphonate ($k_{cat} = 0.1\ s^{-1}$; $K_i = 230\ \mu M$) (*23*) are the only other phosphonates that have been identified as alternate substrates. The various substrate analogues which have been tested (viz., phosphonoacetate, phosphonoethanol, fluorophosphate, acetoacetate, and malonic semialdehyde) bind only weakly to phosphonatase (*23*).

The mechanism of phosphonatase catalysis has been difficult to establish unequivocally. Early investigations showed that catalytic turnover in the presence of the reducing agent borohydride resulted in enzyme inactivation (*10*). At the time, this observation served as solid evidence of a Schiff base mechanism of catalysis. Later it was discovered that the adduct trapped by reduction is not the substrate Schiff base formed from P-Ald but, rather, the Lys53 N^{ϵ}-2-ethylenamine adduct (product Schiff base) (*24*). Protection experiments showed that the Lys53 residue is located at the active site (*24*), and site-directed mutagenesis studies demonstrated that it is essential to catalytic function (*22*). The Lys53 N^{ϵ}-2-ethylenamine adduct was thus considered to be a reaction intermediate, but the actual pathway leading to its formation was unconfirmed. The addition of Lys53 to the P-Ald carbonyl produces an oxyanion, which might abstract a proton and then dehydrate to the Lys53 N^{ϵ}-iminoethylphosphonate adduct. Alternatively, the oxyanion could attack at the phosphorus, to form an oxaphosphetane intermediate (analogous to the oxaphosphetane intermediates formed in Wittig and Horner−Emmons type reactions). As illustrated in Figure 1, upon dephosphonylation both intermediates lead to the observed Lys53 N^{ϵ}-2-ethylenamine adduct.

Lee et al. (*25*) found that phosphonatase-catalyzed hydrolysis of chiral [^{18}O,^{17}O]thiophosphonoacetaldehyde to chiral [^{18}O,^{17}O,^{16}O]thiophosphate occurs with retention of

[1] Abbreviations: AEP, 2-aminoethylphosphonate; HAD, 2-L-haloacid dehalogenase; NCS, noncrystallographic symmetry; MAD, multiwavelength anomalous dispersion; MIR, multiple isomorphous replacement; MLHL, maximum likelihood/Hendrickson−Lattman; Pald, phosphonoacetaldehyde; phosphonatase, phosphonoacetaldehyde hydrolase; rmsd, root-mean square deviation.

configuration at phosphorus. This observation eliminated the mechanism involving the direct in-line attack of water at the phosphonyl group of the Lys53 N^{ϵ}-iminoethylphosphonate adduct (Figure 1b), since this pathway would lead to inversion of configuration at phosphorus. The mechanism proceeding via the oxaphosphetane (Figure 1c) is predicted to occur with retention of configuration at phosphorus (i.e., pseudorotation precedes concerted fragmentation of the C−O and P−O bonds) as is the Schiff-base mechanism (Figure 1a) involving initial transfer of a phosphoryl group to an active-site nucleophile followed by transfer to water. Thus, these latter two mechanisms remained in contention.

To distinguish between the two mechanisms in Figure 1a and 1c, an ^{18}O-labeling experiment was performed (*26*). The phosphate derived from dephosphonylation of the oxaphosphetane intermediate (Figure 1c) would contain the oxygen atom from the P-Ald C═O, while the phosphate derived from hydrolysis of the phosphoenzyme intermediate (Figure 1a) would contain the oxygen derived from a solvent water molecule. Lee (*26*) showed that phosphate produced by phosphonatase-catalyzed hydrolysis of [C(2)-^{18}O]P-Ald in water is devoid of the ^{18}O-label. This result eliminates the oxaphosphetane pathway provided that oxygen exchange had not occurred between the [C(2)-^{18}O]P-Ald and the [^{16}O]H_2O prior to dephosphonylation. While solvent exchange in the absence of enzyme was easily ruled out (*26*), the technical difficulties associated with measuring solvent exchange in the presence of the enzyme proved to be insurmountable (unpublished observations). Therefore, a different approach, focusing on the detection of the phosphoenzyme intermediate, was pursued.

The first line of evidence supporting the intermediacy of a phosphoenzyme in phosphonatase catalysis was derived from protein sequence analysis (*22*). Specifically, phosphonatase was found to possess the same three primary sequence motifs of the L-2-haloacid dehalogenase (HAD) enzyme superfamily (*22*, *27*, *28*), one of which contains a stringently conserved Asp residue that functions in nucleophilic catalysis [i.e., to form an alkylated enzyme adduct in the dehalogenase (*29*) and a phosphoenzyme adduct in the phosphatases (*30*)]. By analogy, Asp12 in phosphonatase was implicated as the phosphoryl acceptor from the Lys53 N^{ϵ}-iminoethylphosphonate intermediate. In this paper, we show by site-directed mutagenesis that Asp12 is essential to phosphonatase catalysis, and by X-ray crystallographic structure determination of the *B. cereus* phosphonatase−Mg(II)−tungstate complex, that Asp12 is properly positioned to accept the phosphoryl group from the Lys53 N^{ϵ}-iminoethylphosphonate donor. A catalytic mechanism, consistent with the X-ray crystallographic data and the solution data, is proposed.

A comparison of the three-dimensional structure of phosphonatase with the three-dimensional structures of the dehalogenase from *Pseudomonas* sp. YL and *Xanthobacter autotrophicus* (*31*, *32*) has now confirmed the common ancestry suggested by the conservation of the three sequence motifs (*22*). Other members of the HAD enzyme superfamily (viz., P-type ATPases, phosphatases, and β-phosphoglucomutases) function, with the assistance of a divalent metal ion cofactor, in P−O bond cleavage. Until now, the link between the catalytic mechanisms of the superfamily members acting on carbon centers and of those acting on phosphorus centers has remained equivocal, despite an ambitious effort to use family sequence data in conjunction with the nonhomologous CheY structure to make the connection (*33*). In the present study, the active-site scaffold common to the P−C bond-cleaving phosphonatase and the C−O bond-cleaving dehalogenases was analyzed in the context of the HAD superfamily structures and sequences to reveal a feasible strategy for catalytic diversification. Preliminary abstracts of this work have been presented (*34*, *35*).

MATERIALS AND METHODS

Preparation of Wild-Type and Asp12Ala Phosphonatase. The wild-type *B. cereus* enzyme was prepared using the *E. coli* clone as described in (*22*). The Asp12Ala mutant gene was generated by the polymerase chain reaction using the plasmid pET-3a, containing the wild-type phosphonatase gene, as the template (*22*). Asp12Ala phosphonatase was prepared in a yield of 5 mg/g of cell paste using the same protocol employed for the wild-type enzyme. The Asp12Ala phosphonatase catalytic activity was measured at a concentration of 50 μM using the standard assay solution containing 1 mM P-Ald, 5 mM $MgCl_2$, 0.13 mM NADH, and 9 units/mL alcohol dehydrogenase in 50 mM K^+HEPES (pH 7.0; 25 °C). The CD spectra of wild-type and Asp12Ala phosphonatase were measured (by the Protein and Carbohydrate Facility of the University of Michigan) at a concentration of 0.1 mg/mL in 5 mM potassium phosphate buffer (pH 7.0).

Inhibition by Tungstate. The K_i of Na_2WO_4 was determined by measuring the initial velocity of phosphonatase-catalyzed hydrolysis of P-Ald as a function of substrate concentration (25−300 μM) and tungstate inhibitor concentration (0, 40, 80, and 100 μM). Reaction solutions containing 5 mM $MgCl_2$ and 100 mM K^+HEPES (25 °C; pH 7.0) were monitored at 340 nm using the alcohol dehydrogenase/NADH continuous spectrophotometric assay described previously (*36*). The K_i value was calculated from the initial velocity data by using the rate equation for competitive inhibition:

$$v = VS/[K_m(1 + I/K_i) + S] \quad (1)$$

where v is the initial velocity, V is the maximal velocity, S is the concentration of the substrate, K_m is the Michaelis constant for the substrate, and I is the concentration of the inhibitor.

Crystallization, Data Collection, and Heavy Atom Screening. Crystallization, data collection, and heavy atom screening were described previously (*37*). To summarize, a search for crystallization conditions produced platelike crystals which diffract to 2.7 Å and were suitable for X-ray analysis. The optimized crystallization conditions were 30% PEG 4000, 100 mM Tris-HCl, pH 7.4, and 100 mM $MgCl_2$. Crystals grown under such conditions are monoclinic, belonging to spacegroup *C2*, with unit cell dimensions a = 210 Å, b = 45 Å, c = 64 Å, and β = 105°. Crystal density was determined using a ficoll gradient (*38*) in order to confirm the number of molecules per asymmetric unit as 2. A native data set to 2.7 Å resolution was collected on such crystals. Additional data sets to at least 3.0 Å were collected on crystals soaked in the following solutions: 10 mM Na_2WO_4, 1 mM ethylmercury phosphate, 1 mM potassium hexachloroiridate, and 1 mM trimethyllead acetate, as well

Table 1: Crystallographic Statistics

(A) Data Collection[a]

crystal	resolution (Å)	no. of unique reflections	% complete	R_{merge}[b]	$\langle I/\sigma \rangle$
W ($\lambda_1 - \lambda_3$)[c]	3.0	25521	93.7 (92.0)[d]	0.215	6.6 (2.0)[d]

(B) Heavy Atom Statistics for MIR Phasing

derivative	R_{iso}[e]	no. of sites	resolution range (Å)	R_c[f]	fh/E[g] (acentrics)	fh/E[g] (centrics)
W	0.179	2	20.0−3.0	0.72	0.61	0.68
Hg	0.150	2	20.0−3.0	0.72	0.52	0.54
Ir	0.179	2	20.0−3.0	0.56	1.23	1.36

[a] Overall figure of merit for MAD phasing (before density modification) = 0.41 (0.59 at 4 Å). [b] $R_{merge} = 100 \times \sum_h \sum_i (|F^2_{hi} - \langle F^2_h \rangle|)/\sum_h \sum_i$, where F^2_{hi} is the square of the ith intensity measurement of reflection h and $\langle F^2_h \rangle$ is the mean squared intensity of the reflection. [c] Data set consisting of all three wavelengths merged together ($\lambda_1 = 1.214698$ Å, $\lambda_2 = 1.2142318$ Å, $\lambda_3 = 1.196994$ Å). [d] Numbers in parentheses represent the value for the highest resolution shell. [e] R_{iso} = mean fractional isomorphous difference = $\sum|F_{ph} - F_p|/\sum F_p$, where F_{ph} and F_p are the derivative and native structure factors, respectively. For MAD analysis, R is calculated between data sets at two different wavelengths for dispersive differences, or between F^+ and F^- at a particular wavelength for anomalous differences. [f] $R_c = \sum|F^H_{obs} - F^H_{calc}|/\sum F^H_{obs}$, where F^H_{obs} and F^H_{calc} are the observed and calculated structure factors, respectively. [g] fh/E = phasing power where fh is the root-mean-square calculated heavy-atom structure factor and E is the root-mean-square lack of closure error.

as a 2.4 Å data set collected on crystals grown in the presence of the competitive inhibitor vinyl sulfonate (5 mM). Data collection statistics are summarized in Table 1. Soaking in heavy metals caused the unit cell edge *c* to double in length. Thus, to circumvent complications introduced by nonisomorphism of the native and vinyl sulfonate data sets with the heavy atom derivatives, the heavy atom data set with the lowest mean isomorphous difference with native, trimethyllead acetate was selected for use as a pseudo-native data set. To further circumvent nonisomorphism problems, a three-wavelength MAD data set was collected to 3 Å resolution on a crystal soaked in 10 mM Na_2WO_4, which was isomorphous with crystals used in the MIR experiment. Independent phase sets were first calculated and refined for the MAD and MIR experiments separately, and then combined by adding the Hendickson−Lattman coefficients. The combined phase distribution was applied to amplitudes obtained from merging the three wavelengths collected in the tungstate MAD experiment. The merging of all three wavelengths of data yields high measurement redundancy, but also increases the calculated *R*-merge (*39*). The final phasing statistics are summarized in Table 1.

Model Building and Refinement. Electron density modification, map calculation, and other data manipulations were carried out using the CCP4 program suite (*40*). Density modification procedures employed included solvent flattening, histogram matching, skeletonization, noncrystallographic symmetry averaging, and multi-crystal averaging. Multi-crystal averaging was performed over the following data sets: (1) the Na_2WO_4 data set phased by MAD, (2) the trimethyllead acetate data set phased by MIR, (3) the native data set, and (4) the enzyme−vinyl sulfonate complex data set. Electron density maps were displayed using the graphics program O (*41*). The resulting density-modified map allowed for unambiguous identification of most of the secondary structure elements in the larger "core" domain (residues 5−20 and 100−266). At this point, density corresponding to the smaller "cap" domain was uninterpretable (residues 20−99).

The program O (*41*) was used to build a partial Cα backbone, and a polyalanine molecule was subsequently built into the density corresponding to the "core" domain. Phases were calculated from this partial model using the ***SFALL*** program in the ***CCP4*** package. This phase probability distribution was weighted, and combined with the original, experimental phase distribution using the ***SIGMAA*** program in the ***CCP4*** package. Density modification on this combined phase distribution produced a map where most of the side chains of the secondary structure elements of the "core" domain were visible, as well as several of the Cα atoms of the secondary structure elements of the smaller cap domain. A new phase set was calculated from this updated model, combined with the original, experimental phase distribution, density-modified, and an additional model was built into the resulting electron density map as described above. This procedure was repeated until a model corresponding to the "core" region of the protein was complete (i.e., main chain and side chain atoms for both secondary structure elements and loop regions had been built), and ∼60% of the smaller "cap" domain had been built (∼48 out of 80 residues).

Model refinement procedures included rigid-body refinement, simulated annealing using torsional dynamics, and *B*-factor refinement as implemented in CNS (*42*), excluding 7% of the data for statistical cross-validation purposes (calculation of R_{free}) (*43*). A maximum likelihood/Hendrickson−Lattman (MLHL) minimization target was utilized for all refinement procedures. Several iterative cycles of simulated annealing procedures followed by manual rebuilding using sigma-weighted (*44*) $2F_o - F_c$ and $F_o - F_c$ difference maps resulted in a final model incorporating 256 out of 266 possible amino acids. Residues 1−4 and 261−266 were not visible in the electron density map and were omitted from the final model. The automated water picking program implemented in CNS was used to assign 16 water molecules in the asymmetric unit (4 waters/monomer). All waters selected were visible in a $F_o - F_c$ map contoured at 3σ and form at least one potential hydrogen bond to the protein and were all located in the active site. At this point, group *B*-factors were refined, resulting in final crystallographic *R* values of $R_{cryst} = 0.248$ and $R_{free} = 0.284$. Analysis of the Ramachandran plot of the final model shows that 80.0% of the 256 residues fall within the most favored region, 17.6% in the additionally allowed region, and only 2.0% in the generously allowed regions, as defined by PROCHECK (*45*). Refinement statistics and final model geometry are summarized in Table 2.

Table 2: Refinement Statistics and Stereochemical Quality of Final Model

final *R* factor (100.0−3.0 Å, working set)	0.248
free *R* factor (100.0−3.0 Å, 7% test set)	0.284
average *B*-factor (Å^2)	24.24
no. of reflections recorded	38774
no. of reflections used in refinement	17343
estimated coordinate error (Å)	0.42
rms deviations from ideality	
bond lengths (Å)	0.009
bond angles (deg)	1.56
dihedral angles (deg)	21.53
improper angles (deg)	1.04

RESULTS AND DISCUSSION

Phosphonatase Inhibition by Tungstate. For the phosphonatase structure determination, tungstate (WO_4^{2-}), a common phosphate analogue, was used to identify the phosphate binding site. To ensure that tungstate had indeed bound at the phosphonatase active site, it was tested as a competitive inhibitor versus the substrate P-Ald. The K_i of tungstate measured as a competitive inhibitor is 50 μM. The tight binding of tungstate to the phosphate site may be attributed to the polarizability of the tungsten atom.

Phosphonatase Tertiary Structure. The crystal structure of the phosphonatase−Mg(II)−tungstate complex at 3.0 Å resolution reveals a dimer of 266 residue (256 observed) subunits related by a 2-fold axis of symmetry. Each "kidney bean" shaped monomer (dimensions: 60 × 45 × 30 Å; Figure 2a) is comprised of 6 β-strands (β1−β6 in Figure 2b) and 12 α-helices (α1−α12 in Figure 2b), which are organized into 2 distinct domains: a larger "core" domain (residues 5−20 and 100−260), and a smaller "cap" domain (residues 21−99). The core domain has an α/β-type structure, distinct from the α/β-hydrolase fold, consisting of a centrally located six-stranded parallel β-sheet (β4-β3-β1-β5-β6-β7) surrounded by seven α-helices. Typical right-handed β-α-β connectivity is observed between β-strands although the location of the switch point, between β3 and β4, is unusual. The "cap domain" is inserted between the first β-strand (β1) and the first α-helix (α6) of the core domain through two flexible, solvent-accessible linker regions [residues 20−24 (L1) and 99−104 (L2)]. The cap domain consists of an antiparallel, five-helix bundle. Helices α1, α3, and α4 are all approximately three-turn helices, whereas α2 and α5 are two- and five-turn helices, respectively. Helices α2 and α3 and the short loop between them point toward the core domain of the protein and form half of the subunit interface. The residues that make up the other half of the subunit interface are positioned on loops connecting the secondary structural elements within the core domain. The structure is well defined with an average temperature (*B*-factor) of 24.2 for main-chain and side-chain atoms (see Table 2). The average *B*-factor for the small cap domain (27.9) is slightly higher than that of the large core domain (22.5), which may be the result of an increased mobility and fewer crystal contacts (6 out of 23 total per dimer) in the cap domain.

Phosphonatase Quaternary Structure. In solution both native and recombinant *B. cereus* phosphonatases are homodimeric enzymes (*22*). The two monomers that make up the dimer observed in the crystal are related by a noncrystallographic 2-fold axis of symmetry (Figure 3a). The side chains from residues comprising α8 from the core domain contribute to the dimer interface where the principal stabilizing interactions are hydrophobic. These interactions include Tyr176 from monomer A with Tyr162, and Trp164 from monomer B, Met171 from monomer A with Met171 from monomer B, Tyr167 from monomer A with Tyr167 from monomer B, Trp164 from monomer A with Tyr176 from monomer B, and Tyr162 from monomer A with Tyr176 from monomer B (representative region shown in Figure 3b with corresponding electron density). The interacting residues at the dimer interface are all within 4 Å of their NCS-related counterparts, a distance that is within reason for hydrophobic interactions. The absence of dimerization would leave a large, solvent-exposed hydrophobic patch on the enzyme. Since such a structure would be energetically unfavorable, this result suggests that the interface stabilizes the true biological dimer as opposed to dimerization induced by crystallization. Additional evidence in support of this conclusion comes from the observation that this same dimer exists in phosphonatase even when the enzyme crystallizes in a different spacegroup (unpublished results).

La Nauze et al. observed that Mg(II) is required for dimerization (*36*). The structure shows that Mg(II) is not present at the dimer interface, and if it were, its presence in this hydrophobic environment would be energetically unfavorable. We are certain that the dimer observed in the crystal is the true biological dimer, and, therefore, it is difficult to account for the reported Mg(II) effect.

Surprisingly, the two monomers comprising the dimer are not identical. Tungstate is bound by only one of the two subunits of the phosphonatase dimer, and the orientation of the cap domain relative to the core domain in the two subunits is different. The change in relative orientation of the two domains stems from changes in the backbone conformation at Leu28 and Phe95, resulting in a hinge-like motion in the two solvated, interdomain linker regions. In the monomer with tungstate bound, the two subdomains are closer together than in the monomer with an unoccupied active site. As a result, the domain−domain interface in the monomer with tungstate bound is tighter than in the unbound monomer. Whether the change in interdomain orientation is related to ligand binding and/or crystal contacts must await the determination of additional structures of phosphonatase.

Phosphonatase Active-Site Residues and Catalysis. The phosphonatase active site is located at the core domain−cap domain interface. The side chains of the contributing active-site residues are pictured in Figure 4. Tungstate and Mg(II) are bound to the core domain in close proximity to Asp12. The Mg(II) ligands include two tungstate oxygens, one oxygen of the carboxylates of Asp12 and Asp186, and the backbone carbonyl oxygen of Ala14. The sixth Mg(II) ligand is a water molecule, positioned to interact favorably with the side-chain carboxylate of Asp190 and the hydroxyl of Thr187. Residue Thr16 is also nearby the Mg(II), and positioned to interact with the Asp12 nucleophile. Residues Asp12, Asp186, Ala14, and Thr16 are stringently conserved among the three known phosphonatase sequences (*22*). In *P. aeruginosa* and *S. typhimirium*, phosphonatase Asp190 is replaced with Gly. These sequences contain Asp185 instead. A simple modeling exercise in which Gly185 in the *B. cereus* enzyme is replaced by Asp demonstrates that if the side-chain position at 185 is retained, the carboxylate

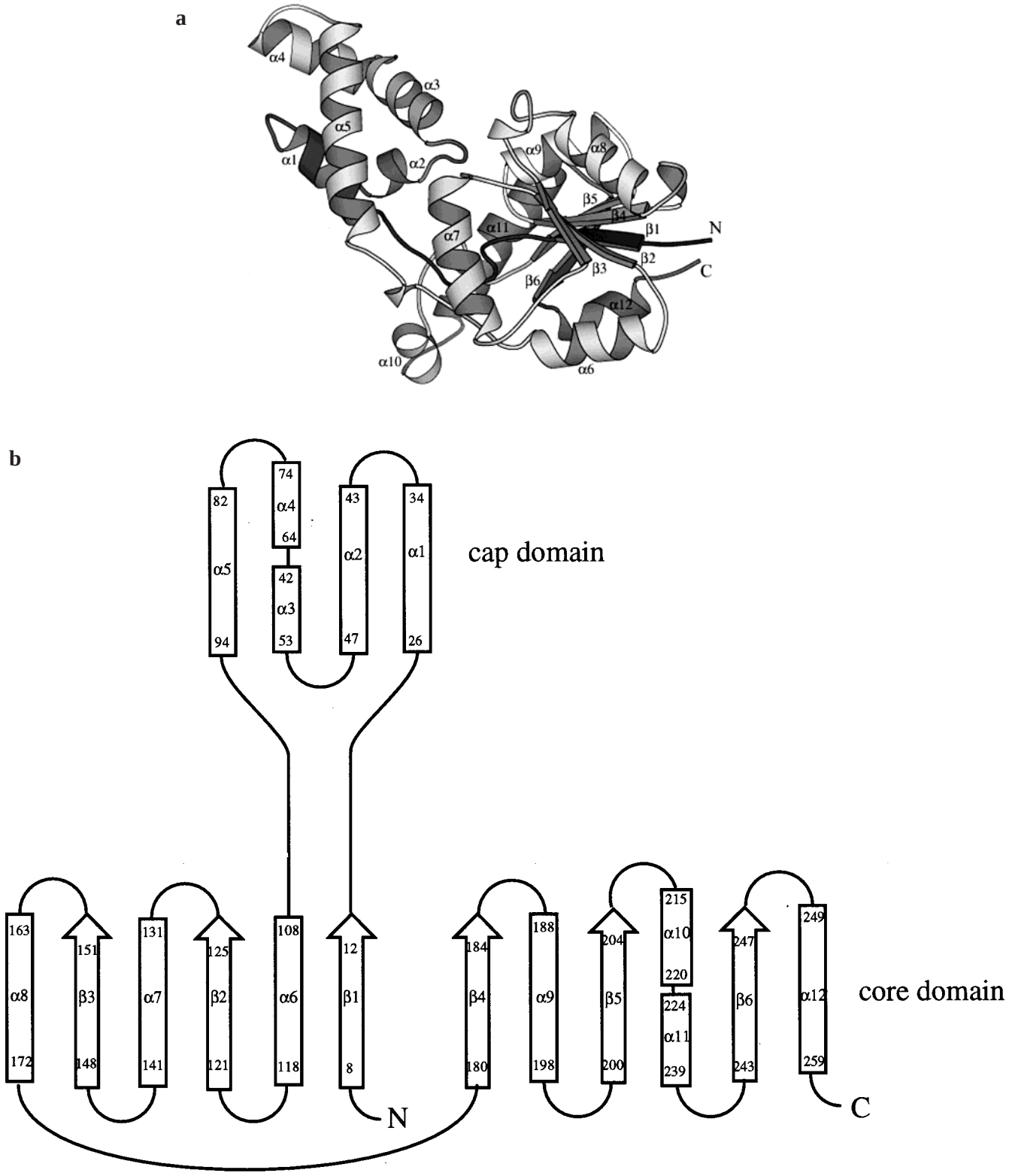

FIGURE 2: Structure of the phosphonatase monomer. (a) The tertiary structure is represented as a ribbon diagram with β-strands shown as arrows and α-helices as coils. This figure was generated using the program Molscript (*53*). (b) The topology of secondary structural elements with α-helices represented as columns and β-strands represented as arrows. Secondary elements and termini are labeled.

group of Asp185 would superimpose with the water held by Asp190 in the *B. cereus* structure. Thus, either Asp185 or an Asp190−water pair serves to ligand Mg(II) in phosphophosphonatase. The tungstate makes bidentate interactions with the Mg(II) and monodentate interactions with the guanidinium of the stringently conserved residue Arg160 as well as the backbone nitrogens of Gly127 and Tyr128. The Arg160 simultaneously interacts with the carboxylate of Asp12 which, in turn, is positioned for in-line attack at the tungsten atom. The side chains of Cys22 and Tyr128 are also located in this region. Tyr128 is conserved but Cys22 is replaced with Ser in the other two phosphonatase sequences. The Lys53 side chain enters the active-site crevice of the core domain from the N-terminus of the α3 helix of

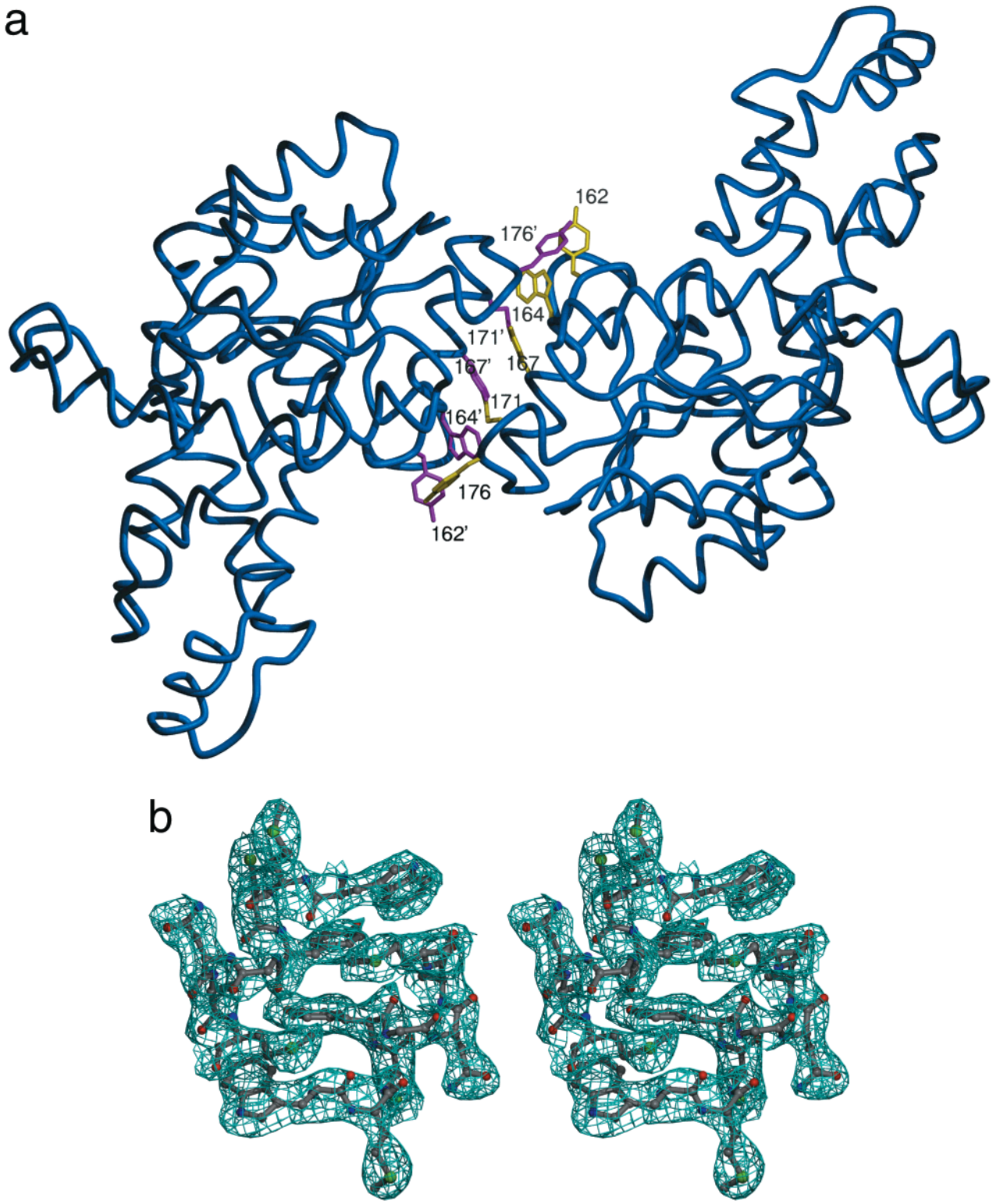

FIGURE 3: Dimer interface of phosphonatase. (a) The backbones of the two phosphonatase monomers are shown as blue coils. Residues involved in the hydrophobic dimer interface (comprised of α8 of the core domain, see Figure 2a) are depicted as licorice whip representations with those contributed from one monomer shown in yellow and those from the second monomer in magenta. (b) Stereoview of representative residues comprising the hydrophobic interface shown as ball-and-stick with corresponding electron density shown as cyan cages (electron density from a $2F_o - F_c$ map contoured at 1.0σ). This figure was rendered using the programs Molscript (*53*) and POVRAY (*54*).

the cap domain. Closely surrounding the Lys53 side chain are the hydrophobic residues Pro25, Phe29, and Met49 from the cap domain and Phe90 and Leu94 from the cap domain. His56 is positioned on the α3 helix, just behind the Lys53. With the exception of Leu94, these residues are stringently conserved.

The arrangement of ligands and side chains in the phosphonatase active site (Figure 4) provides insight into the mechanism of hydrolytic cleavage in P-Ald. Covalent catalysis by Lys53 had been implicated by reductive trapping of the Lys53−N^{ϵ}-2-ethylenamine adduct generated under steady-state conditions (*24*). Amino acid replacement of the

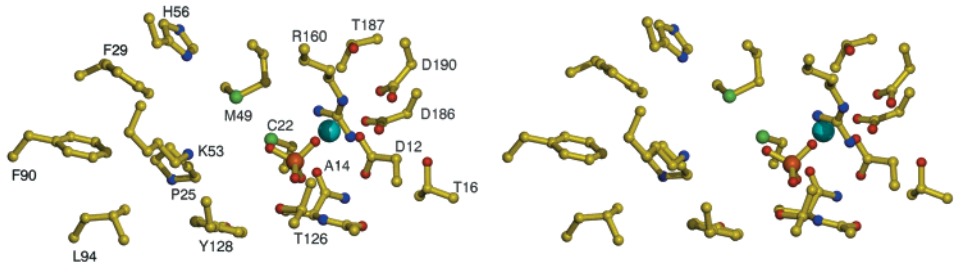

FIGURE 4: Stereoview of the active site of phosphonatase. The Mg(II) ion is shown as a cyan sphere, the tungstate is shown as a ball-and-stick with an orange tungsten atom, and enzyme residues are shown as ball-and-stick representations. This figure was rendered using the programs Molscript (*53*) and POVRAY (*54*).

Lys53 removed all catalytic activity, indicating the formation of the covalent adduct between P-Ald and Lys53 is essential to the overall reaction (*22*). In the present structure, Lys53 comprises part of the active site through the close association of the cap domain with the core domain. The Lys53 N^{ϵ} is positioned directly above the bound tungstate. By modeling the phosphonate group of P-Ald in place of the tungstate (data not shown), we find that the substrate carbonyl group is positioned within striking distance of the Lys N^{ϵ}. This observation leaves little doubt that the first step of phosphonatase catalysis involves attack of the Lys53 N^{ϵ} on the P-Ald C=O.

To function as a nucleophile, Lys53 must be neutral at operating pH. The pH−rate profiles measured for phosphonatase inactivation with acetic anhydride show an ionizing group with a pK_a of ~6.0 (*23*). This pK_a has been assigned to Lys53 although the possibility cannot be excluded that another active-site moiety is the ionizing group. A pK_a of 6.0 is ~4 pH units lower than that of a solvated lysine residue. A depression of this magnitude has been noted previously for the Schiff base-forming Lys of the enzyme acetoacetate decarboxylase [pK_a = 5.9 (*46*, *47*)]. Based on the primary structure of the decarboxylase which shows that the catalytic Lys residue is juxtaposed to a second Lys, it has been suggested that unfavorable charge−charge interactions are responsible for the pK_a perturbation (*48*, *49*). In phosphonatase, the electrostatic interactions responsible for pK_a depression cannot be attributed to a single point charge but are probobly the result of several electrostatic effects. The Lys53 resides at the N-terminus of the α3 helix of the cap domain, where it is likely to be influenced by the electropositive field of the helix dipole [as previously reported for triosephosphate isomerase (*50*)]. The hydrophobic active-site microenvironment of the phosphonatase Lys53 created by the side chains of Pro25, Phe29, Met49, Phe90, and Leu94 may also serve to destabilize the charged N^{ϵ}. This hypothesis depends on the assumption that the proton can leave the microenvironment.

The addition of Lys53 to the P-Ald C=O results in the formation of an oxyanion, which could either pick up a proton in route to dehydration to an imine (Schiff base) adduct or, alternatively, attack the phosphorus to form an oxaphosphetane intermediate. As illustrated in Figure 1, and discussed in the introduction, all pathways converge at the Lys53 N^{ϵ}-2-ethylenamine adduct, identified by borohydride trapping (*24*). Stereochemical studies ruled out a pathway involving direct attack of water at the substrate Schiff base (Figure 1b) while ^{18}O-labeling experiments provided conditional evidence against a pathway proceeding via an oxaphosphetane intermediate (Figure 1c). The pathway remaining, unique in its formation of a bicovalent enzyme intermediate, had thus emerged as the center of focus. The connection that was ultimately made between phosphonatase and the HAD enzyme superfamily identified Asp12 as the probable phosphoryl group acceptor (*22*). In the present study, Asp12 was replaced with Ala, a residue that is not able to function as the phosphoryl group acceptor. There were no noticeable differences in the chromatographic behavior of wild-type and mutant enzyme, and CD spectra of the two proteins were essentially identical (trough centered at 219 nm: molar elipticity = −200 000). Using a coupled assay to detect acetaldehyde, no product formation was observed over a 3 h period, indicating the turnover rate of the mutant enzyme is less than 1×10^{-5} s^{-1}. Thus, the Asp12Ala phosphonatase mutant folds into a soluble nativelike protein but is inactive, indicating that Asp12 is essential to catalytic function. The present crystal structure shows that Asp12 is located in the phosphonatase active site, close to the bound tungstate and Mg(II) ligands. Assuming that tungstate binds at or near the P-Ald phosphonate binding site, then the Asp12 is well positioned for in-line attack at the phosphorus. In future studies, transient kinetic methods will be employed to confirm the intermediacy of the Asp12-acyl phosphate.

The formation of the acyl phosphate intermediate is facilitated by Mg(II) and Arg160 which, by binding to both the Asp12 nucleophile and the Lys53 N^{ϵ}-iminoethylphosphonate electrophile, can orient them for reaction and minimize unfavorable charge−charge interactions occurring between them. The active-site residues which participate in the acid/base chemistry that leads to the formation of the Lys53 N^{ϵ}-iminoethylphosphonate and hydrolysis of the Asp12-acyl phosphate and Lys53 N^{ϵ}-2-ethylenamine adducts are, for present, left unassigned. Tyr128 is available, but exactly what, if any, role it plays in catalysis has yet to be determined. Learning how acid−base catalysis is mediated in the phosphonatase active site must await structure determination of enzyme−substrate and enzyme−product complexes, and site-directed mutagenesis studies of the active-site residues.

Conservation of Fold and Active-Site Scaffold. The level of sequence divergence among members of the HAD enzyme superfamily is so high (sequence identity <15%) that, if it were not for the highly conserved catalytic motifs, the relationship between the family members would go unrecognized. Until now, the only three-dimensional structures representing the family are those of two 2-haloacid dehalogenases [one from *Pseudomonas* sp. strain YL (*31*) and the other from *Xanthobacter autotropicus* GJ10 (*32*)] and a

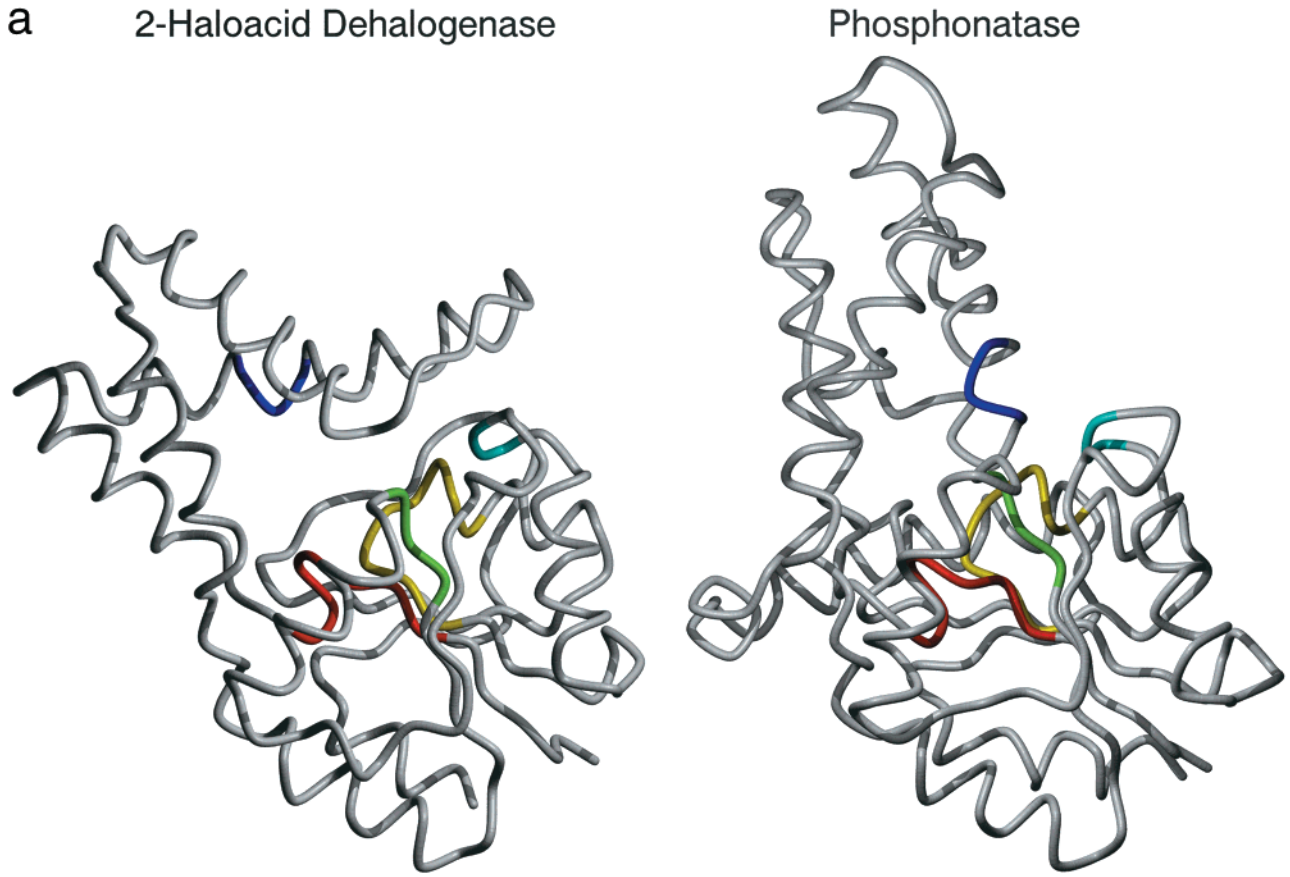

b

	Loop 1	Loop 2	Loop 3	Loop 4	
	12 16	126	160	185 186 190	
IFDWAGTT	17	STTGYTRE	131	GRPYPWM	165 IKVG DTVSDMKEGR 194 Phn.Bc
ILDWAGTT	16	SCSGYPAA	130	GRPGPWM	166 VKVD DAAPGISEGL 196 Phn.St
ILDWAGTV	20	SCSGYPRV	135	GRPWPAQ	171 VKVD DTWPGILEGR 201 Phn.Pa
AFDLYGTL	15	ILSNGSPQ	120	YKPDNRV	156 LFVS SNAWDATGAR 186 Had.P.Yl
VFDAYGTL	12	ILSNGAPD	117	FKPHPDS	135 LFVS SNGFDVGGAK 163 Had.Xa
LFDVDGTL	13	VATTTSLP	120	KKPSPDI	156 VALE DSLNGLRAAK 185 PGP.Rs
VTDIEGTT	13	VYSSGSVA	130	AKREAQS	164 LFLS DIHQELDAAE 193 EP.Ko
CFDVDSTV	114	LISGGFSI	203		IMIG DGATDMEACP 379 PSP.Hs
LLDMDGVM	16	VVTGRPRK	129	KPSPEP	161 M.VG DTVDDIIAGR 190 IGPD.Pp
VFDLDGVL	14	ILTNTWLD	112	VKPEPQI	165 VFLD DIGANLKPAR 196 sEH.Hs
LFDLDGTI	17	IVTSGSPY	123	GKPDPEG	156 VVFE DAPVGIKAGK 192 DGPP.Sc
LFDVDGTI	44	VATSGTRD	141	GKPHPEP	175 VVFE DAPAGIAAGK 211 G3P.Sc
LFDLDGVI	13	LASASKNG	119	SKPAPDI	148 IGLE DSQAGIQAIK 176 PGM.Ll
IFDMDGTL	14	VVSGSKYE	48	SKSIALS	194 FFGD NTREGGNDFE 217 PMM.Bb
ILDKTGTI	430	MVTGDNQR	587	EKANYVE	617 MVGD GINDAPALRL 741 ATP.Eh
CSDKTGTL	392	MVTGDHPI	633	QKLVIVE	714 VTGD GVNDSPALKK 738 ATP.Hs

FIGURE 5: Three-dimensional structures of the dehalogenase from *Pseudomonas* sp. YL and phosphonatase and the HAD superfamily primary sequence alignment. (a) The two enzymes are depicted in the same relative orientation as coils. The loops are color-coded to match the corresponding residues in the (b) superfamily sequence alignment. The positions of the motifs within the sequences are indicated by residue numbers. The sequences shown are as follows with GenBank access codes given in parentheses: Phn.Bc, phosphonatase from *B. cereus* (g2623262); Phn.St, phosphonatase from *S. typhimurium* (U69493); Phn.Pa, phosphonatase from *P. aeruginosa* (45309); Had.P. Yl, 2-haloalkanoic dehalogenase from *Pseudomonas* sp. strain YL (S74078); Had. Xa, 2-haloalkanoic dehalogenase from *Xanthobacter autotrophicus* (q60099); PGP.Rs, 2-phosphoglycolate phosphatase (u67781Y); Ep.Ko, enolase-phosphatase from *Klebsiella oxytosa* (a49101); PSP.Hs, phosphoserine phosphatase from *Homo sapiens* (10275); IGPD.Pp, the N-terminal domain of the putative bifunctional imidizole glycerolphosphate dehydratase:histidinol phosphatase from *Phytophthora parasitica* (Z11591; direct submission to GenBank by P. Karlovsky in 1992); sEH.Hs, epoxide hydrolase from *Homo sapiens* (X97024); DGPP.Sc, 2-deoxyglucose 6-phosphate phosphatase from *Sa. cerevisae* (P38773); G3P.Sc, glycerol-3-phosphate phosphatase from *Sa. cerevisae* (p41277); PGM.Ll, β-phosphoglucomutase from *Lactococus lactis* (Z70730); PMM.Bb, phosphomannomutase from *Babesia bovis* (2731570); ATP.Eh, Cu(II)-ATPase from *Enterococcus hirae* (P32113); ATP.Hs, gastric H^+,K^+-ATPase from *Homo sapiens* (P20648). Panel A was rendered using the programs Molscript (*53*) and POVRAY (*54*).

catalytically inactive domain from soluble epoxide hydrolase (*51*). Not surprisingly, the folds and active-site structures of the two dehalogenases, which differ only in substrate specificity, are quite similar. The question of conservation

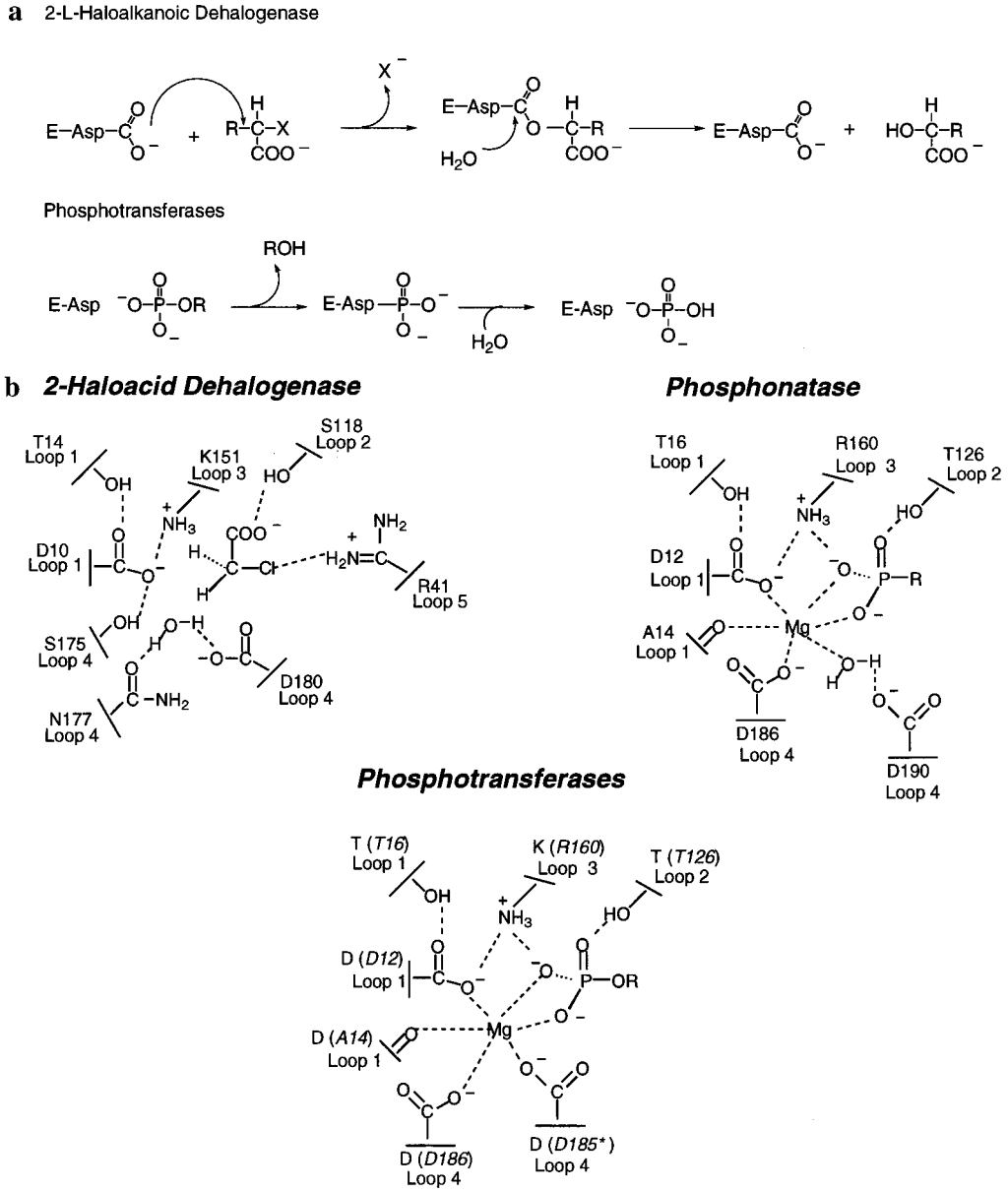

FIGURE 6: General chemical mechanisms of (a) HAD and HAD superfamily phosphotransferases and (b) schematic representations of the active sites of HAD and phosphonatase and the proposed active site of the HAD superfamily phosphotransferases. The loops forming each catalytic station are labeled and described in the text. Residue numbering for HAD is from the *Pseudomonas* sp. YL enzyme, and numbering for phosphonatase is from the *B. cereus* enzyme. For the phosphotransferase model, the corresponding residue in *B. cereus* phosphonatase is given. The residue in loop 4 denoted by an asterisk corresponds to Asp185 (in *P. aeruginosa* and *S. typhimurium* phosphonatase and the phosphotransferases) and corresponds to Asp190 in *B. cereus* phosphonatase.

of backbone fold and active-site diversification within the family is best addressed through comparison of members catalyzing different chemistries. By comparing the folds, active-site scaffolds, and catalytic mechanisms of phosphonatase and 2-haloacid dehalogenase, our intention is to gain insight into the evolution of catalysis within the HAD enzyme superfamily.

The structures of the dehalogenase and phosphonatase monomers are compared in Figure 5. Despite the low overall sequence identity between these enzymes, their folds are remarkably similar, particularly within the core domain (rmsd of 3.9 Å). The similarity in the overall folds of these two enzymes together with the high sequence identity within the conserved catalytic motifs (*22*) supports the hypothesis that they evolved by divergent evolution from a common progenitor. In the case of convergent evolution to a common protein structure and common chemistry, it would be expected that there would be no significant sequence identity and that the catalytic groups would be provided by different loops and therefore different regions of the polypeptide chain (*52*). This is not the case in the dehalogenase and phosphonatase where the conserved core domain supports a common active-site scaffold that consists of four loops located at topological switchpoints of the core domain (as identified in Figure 5a according to color). The fifth active-site segment, which will be referred to as loop 5, is contributed by the cap domain. In phosphonatase, loop 5 contributes the Schiff base forming Lys53 to the active site while in the dehalogenase it provides the Cl^- binding residue Arg41. Because of the high level of divergence existing in cap domain sequences and structures, the discussion of the conserved active-site scaffold within the HAD superfamily

will, for the present, be restricted to the four loops of the core domain.

The catalytic mechanisms operating in phosphonatase and 2-haloacid dehalogenase (see Figure 6a) are well-defined. Therefore, the use of catalytic stations located on the four loops of these two enzymes can be contrasted. Briefly, in phosphonatase loop 1 is used to station Asp12, the nucleophile, as well as Thr16 which orients it for reaction. The same is true for the dehalogenase that (using the numbering system for the *Pseudomonas* sp. YL enzyme) stations Asp10 and Thr14 to serve in analogous roles. Loop 2 of the dehalogenase stations Ser118 to form a hydrogen bond with the carboxylate substituent of the reactant. The corresponding loop in phosphonatase stations Thr126 to form a hydrogen bond with the phosphonate substituent of the reactant. Loop 3 is used in both the dehalogenase and the phosphonatase to position a positively charged group (Lys151 in the dehalogenase and Arg160 in the phosphonatase) to form a salt bridge with the Asp nucleophile. In phosphonatase, Arg160 also interacts with the phosphonyl group of the reactant. In the dehalogenase, Lys151 is used to stabilize the alkoxide leaving group displaced during hydrolysis of the ester intermediate.

It is loop 4 that performs divergent functions in the phosphonatase and the dehalogenase. In *B. cereus* phosphonatase, loop 4 positions Asp186 and Asp190 (through water) or Asp185 to function along with the Asp12 of loop 1 in coordinating a Mg(II) (see Figure 4 for view of the active site). In the absence of the bound Mg(II), the electrostatic repulsion between the three carboxylate ligands would be significant [which may explain why Mg(II) binding is so tight in phosphonatase as evidenced by the fact that the enzyme is denatured when metal is removed (unpublished observations)]. Loop 4 of the dehalogenase positions Ser175 to interact with the Asp nucleophile on loop 1, and Asn177 and Asp180 bind the water molecule that serves in the hydrolysis of the ester intermediate (corresponding to the water bound to phosphonatase Thr187 and Asp190). Thus, in the dehalogenase the loop 4 residues are used to position the Asp nucleophile and hold a water for hydrolysis of the intermediate, while in the phosphonatase the loop 4 residues are used to hold the Mg(II) cofactor either directly or through water. Mg(II) is required in the phosphonatase to shield the charge of the phosphonyl group as it is approached by the charged Asp nucleophile. In the dehalogenase, Asp approaches an electropositive carbon center and, thus, a Mg(II) cofactor is not required. On the other hand, since hydrolysis in the dehalogenase occurs at the carbonyl carbon of the ester intermediate and not at C2, the station that binds Mg(II) in phosphonatase must be used in the dehalogenase to position water for in-line attack. In phosphonatase, hydrolysis at the Asp12-acyl phosphate occurs at the phosphorus, not at the carbonyl carbon. Thus, the attacking water molecule must be positioned differently (i.e., behind the phosphoryl group, in-line with the Asp12 C−O−P).

Based on the above comparison, it is apparent that the divergence in chemistries represented by phosphonatase and 2-haloacid dehalogenase centers on the use of loop 4 in binding a metal cofactor versus a water molecule. In each of the HAD family enzymes that act on phosphate substrates, we anticipate that loop 4 will function in Mg(II) binding and, therefore, that it will station an Asp overlapping in three-dimensional space with position 186 (number based on phosphonatase numbering) and an Asp at position 185 or 190. Inspection of the sequences listed under loop 4 of Figure 5b supports this prediction. Based on the conservation of the key catalytic amino acids of the HAD superfamily, a general picture of the active site of the phosphotransferases from the superfamily (including β-phosphoglucomutase, phosphoserine phosphatase, and the P-type ATPases) can be constructed (Figure 6b). This general phosphotransferase model can be constructed simply by substituting the conserved amino acids of the phosphotransferases for the corresponding amino acids in phosphonatase using the HAD superfamily sequence alignment. Thus (using phosphonatase numbering), the nucleophilic Asp12, stabilizing residues Thr16 and Thr126, as well as the salt bridge forming Lys or Arg160 are all retained in the phosphotransferases. Also retained are the two Mg(II) ligands Asp185 and Asp186. It is tempting to speculate that in the phosphate ester hydrolases and mutases, the carboxylate positioned at position 14 two residues down from the Asp nucleophile is used as the acid/base catalyst while in the P-type ATPases, the Asp residue positioned on loop 2 (at the position corresponding to the Tyr128 in phosphonatase) is employed in base catalysis.

Conclusion. The structure of phosphonatase from *B. cereus* determined to 3.0 Å resolution is consistent with a mechanism utilizing the active-site nucleophile Asp12 to abstract the phosphoryl group from the Schiff-base intermediate formed from Lys53 and P-Ald. This is the first example of bicovalent catalysis by an enzyme on a single substrate. The fold of phosphonatase supports the evidence from primary sequence alignment that phosphonatase shares ancestry with the enzymes of the HAD superfamily, in that the domain that supports the common chemistry is conserved between the dehalogenase and phosphonatase. From an analysis of the conserved active sites, it can be seen that loop 4 has been recruited by phosphonatase, and, by extension, by the phosphotransferase members of the superfamily (including β-phosphoglucomutase, phosphoserine phosphatase, and the P-type ATPases), as a metal binding site to allow nucleophilic substitution at charged substrates.

REFERENCES

1. Abe, S., Araki, S., Sataka, M., Fujiwara, N., Kon, K., and Ando S. (1991) *J. Biol. Chem. 266*, 9939.
2. Yamaguchi, Y., Ohta, M., and Hayashi, A. (1992) *Biochim. Biophys. Acta 1165*, 160.
3. Mohan, M. S., and Abbott, E. H. (1978) *J. Coord. Chem. 253*, 175.
4. Hendlin, D., Stapley, E. O., Jackson, M., Wallick, H., Miller, A. K., Wolf, F. J., Miller, T. W., Chaiet, L., Kahan, F. M., Foltz, E. L., Woodruff, H. B., Mata, J. M., Hernandez, S., and Mochales, S. (1969) *Science 166*, 122.
5. Steiner, S., Conti, S. F., and Lester, R. L. (1973) *J. Bacteriol. 116*, 1199.
6. Egli, T. (1988) *Microbiol. Sci. 5*, 36.
7. Wackett, L. P., Shames, S. L., Venditte, C. P., and Walsh, C. T. (1987) *J. Bacteriol. 169*, 710.
8. Shames, S. L., Wackett, L. P., Labarge, M. S., Kuczkowski, R. L., and Walsh, C. T. (1987) *Bioorg. Chem. 15*, 336.
9. Chen, C. M., Ye, Q. Z., Zhu, Z. M., Wanner, B. L., and Walsh, C. T. (1990) *J. Biol. Chem. 265*, 4461.
10. LaNauze, J. M., Coggins, J. R., and Dixon, H. B. F. (1977) *Biochem. J. 165*, 409.
11. McMullan, G., Harrington, F., and Quinn, J. P. (1992) *Appl. Environ. Microbiol. 58*, 1346.

12. Ternan, N. G., McGrath, J. W., and Quinn, J. P. (1998) *Appl. Environ. Microbiol. 64*, 2291.
13. La Nauze, J. M., and Rosenberg, H. (1968) *Biochim. Biophys. Acta 165*, 438.
14. Lacoste, A. M., and Neuzil, E. (1969) *C. R. Seances Acad. Sci., Ser. D 269*, 254.
15. Dumora, C., Lacoste, A.-M., and Cassaigne, A. (1989) *Biochim. Biophys. Acta 997*, 193.
16. Lee, K. S., Metcalf, W. W., and Wanner, B. L. (1992) *J. Bacteriol. 174*, 2501.
17. Jiang, W., Metcalf, W. W., Lee, K. S., and Wanner, B. L. (1995) *J. Bacteriol. 177*, 6411.
18. Ternan, N. G., and Quinn, J. P. (1998) *Biochem. Biophys. Res. Commun. 248*, 378.
19. Parker, G. F., Higgins, T. P., Hawkes, T., and Robson, R. L. (1999) *J. Bacteriol. 181*, 389.
20. Kim, A., Kim, J. B., and Dunaway-Mariano, D. (1998) *J. Biol. Chem. 273*, 4443.
21. Tan, S. A., and Tan, L. G. (1989) *Clin. Physiol. Biochem. 7*, 303.
22. Baker, A. S., Ciocci, M. J., Metcalf, W. W., Kim, J., Babbitt, P. C., Wanner, B. L., Martin, B. M., and Dunaway-Mariano, D. (1998) *Biochemistry 37*, 9305.
23. Olsen, D. B., Hepbern, T. W., Lee, S.-L., Martin, B. M., Mariano, P. S., and Dunway, D.-M. (1992) *Arch. Biochem. Biophys. 296*, 144.
24. Olsen, D. B., Hepburn, T. W., Moos, M., Mariano, P. S., and Dunway, D.-M. (1988) *Biochemistry 27*, 2229.
25. Lee, S.-L., Hepburn, T. W., Swartz, W. H., Ammon, H. L., Mariano, P. S., and Dunaway-Mariano, D. (1992) *J. Am Chem. Soc. 114*, 7346.
26. Lee, S.-L. (1991) Ph.D. Thesis, University of Maryland.
27. Koonin, E. V., and Tatusov, R. L, (1994) *J. Mol. Biol. 244*, 125.
28. Aravind, L., Galperin, M. Y., and Koonin, E. V. (1998) *Trends Biochem. Sci. 23*, 127.
29. Liu, J. Q., Kurihara, T., Miyagi, M., Esaki, N., and Soda, K. (1995) *J. Biol. Chem. 270*, 18309.
30. Collet, J. F., Gerin, I., Rider, M. H., Veiga-da-Cunha, M., and Van Schaftingen, E. (1997) *FEBS Lett. 408*, 281.
31. Hisano, T., Hata, Y., Fujii, T., Liu, J.-Q., Kurihara, T., Esaki, N., and Soda, K. (1996) *J. Biol. Chem. 271*, 20322.
32. Ridder, I. S., Rozeboom, H. J., Kalk, K. H., Janssen, D. B., and Dijkstra, B. W. (1997) *J. Biol. Chem. 272*, 33015.
33. Ridder, I. S., and Dijkstra, B. W. (1999) *Biochem. J. 339*, 223.
34. Allen, K. N., Mazurkie, A. S., Morais, M. C., Baker, A. S., and Dunaway-Mariano, D. (1998) *FASEB J. 12*, 132.
35. Morais, M. C., Zhang, W., Dunaway-Mariano, D., and Allen, K. N. (1999) *Protein Sci. 8, Suppl. 1*, 145.
36. La Nauze, J. M., Rosenberg, H., and Shaw, C. (1970) *Biochim. Biophys. Acta 212*, 332.
37. Morais, M. C., Baker, A. S., Dunaway-Mariano, D., and Allen, K. N. (1999) *Acta Crystallogr. D56*, 206.
38. Westbrook, E. M. (1985) *Methods Enzymol. 114*, 187.
39. Diederichs, K., and Karplus, P. A. (1997) *Nat. Struct. Biol. 4*, 269.
40. Collaborative Computational Project, Number 4 (1994) *Acta Crystallogr. D50*, 760.
41. Jones, T. A., Zou, J. Y., Cowan, S. W., and Kjeldgaard, M. (1991) *Acta Crystallogr. A47*, 110.
42. Brünger, A. T., Adams, P. A., Clore, G. M., DeLano, W. L., Gros, P., Grosse-Kuntsleve, R. W., Jiang, J.-S, Kuszewski, J., Nilges, M., Pannu, N. S., Read, R. J., Rice, L. M., Simonson, T., and Warren, G. L. (1998) *Acta Crystallogr. D54*, 905.
43. Brünger, A. T (1992) *Nature 355*, 472.
44. Read, R. J. (1997) *Methods Enzymol. 274*, 110.
45. Laskowski, R. A., MacArthur, M. W., Moss, D. S., and Thornton, J. M. (1993) *J. Appl. Crystallogr. 26*, 283.
46. Frey, P. A., Kokesh, F. C., and Westheimer, F. H. (1971) *J. Am. Chem. Soc. 93*, 7266.
47. Kokesh, F. C., and Westheimer, F. H. (1971) *J. Am. Chem. Soc. 93*, 7270.
48. Laursen, R. A., and Westheimer, F. H. (1966) *J. Am. Chem. Soc. 88*, 3426.
49. Highbarger, L. A., Gerlt, J. A., and Kenyon, G. L. (1996) *Biochemistry 35*, 41.
50. Lodi, P. J., and Knowles, J. R. (1993) *Biochemistry, 32*, 4338.
51. Argiriadi, M. A., Morisseau, C., Hammock, B. D., and Christianson, D. W. (1999) *Proc. Natl. Acad. Sci. U.S.A. 96*, 10637.
52. Branden, C., and Tooze, J. (1991) in *Introduction to Protein Structure*, p 48, Garland Publishing, New York.
53. Kraulis, P. J. (1991) *J. Appl. Crystallogr. 24*, 946.
54. Persistence of Vision Ray Tracer (POV−Ray) Version 3.01.

BI001171J